

# Implementation of a Simple Actuator Disc for Large Eddy Simulation in the Weather Research and Forecasting Model (WRF-SADLES-V1.2) for Wind Turbine Wake Simulation

Hai Bui<sup>1,2</sup>, Mostafa Bakhoday-Paskyabi<sup>1,2</sup>, and Mohammadreza Mohammadpour-Penchah<sup>1,2</sup>

<sup>1</sup>Geophysical Institute, University of Bergen, Allégaten 70, 5007 Bergen, Norway

<sup>2</sup>Bergen Offshore Wind Centre, Allégaten 55, 5007 Bergen, Norway

**Correspondence:** Hai Bui (hai.bui@uib.no)

**Abstract.** In this study, we present the development of a Simple Actuator Disc model for Large Eddy Simulation (SADLES), implemented within the Weather Research and Forecast (WRF) model, which is widely used in atmospheric research. The WRF-SADLES model supports both idealized studies and realistic applications through downscaling from realistic data, with a focus on resolutions of tens of meters. Through comparative analysis with the Parallelized Large-eddy Simulation Model (PALM) at resolutions of 10 meters and 30 meters, we validate the effectiveness of WRF-SADLES in simulating the wake characteristics of a 5-MW wind turbine. Results indicate good agreement between WRF-SADLES at 30-meter resolution, 10-meter resolution, and the PALM model. Additionally, we demonstrate a practical case study of WRF-SADLES by downscaling ERA5 reanalysis data using a nesting method to simulate turbine wakes at the Alpha Ventus wind farm in the South of the North Sea. The meso-to-micro downscaling simulation reveals that the wake effect simulated by WRF-SADLES at the FINO1 offshore meteorological mast station aligns well with the cup anemometer and LiDAR measurements. Furthermore, we investigate an event of farm-to-farm interaction, observing a 16% reduction in ambient wind speed and a 38% decrease in average turbine power at Alpha Ventus due to the presence of a wind farm to the southwest. WRF-SADLES offers a promising balance between computational efficiency and accuracy for wind turbine wake simulations, making it valuable for wind energy assessments and wind farm planning.

## 15 1 Introduction

Wind energy has become increasingly important due to the pressing need to address climate change and reduce our reliance on fossil fuels. It is crucial to have a deep understanding of the complex interaction between wind turbines and the atmospheric boundary layer (ABL) for effective wind energy assessment and wind farm construction planning. In particular, the wake created behind upstream turbines can have a significant impact on the performance of downstream turbines, resulting in reduced power production and increased turbulence (Porté-Agel et al., 2020; Bakhoday-Paskyabi et al., 2022a). Large eddy simulation (LES) is a powerful tool that can simulate ABL turbulence with high spatial and temporal resolution, making it an invaluable resource for studying turbine wakes and their interaction with the ABL (Breton et al., 2017).

To model the turbine wakes, various methods exist with different levels of accuracy and computational cost. The most accurate, but computationally expensive, are the Actuator Surface (AS) and Actuator Line (AL) models. These models typically 25 employ Blade Element (BE) theory (Burton et al., 2011) to calculate the thrust and torque on the turbine blades. A less computationally demanding approach is the Actuator Disc with Rotation (AD+R) model. This model represents the turbine blades as a permeable disc extracting energy from the wind through axial and azimuthal forces. AD+R models often utilize BE theory or combine it with momentum theory (i.e. BEM theory, Göçmen et al., 2016; Ledoux et al., 2021). The simplest form is the actuator disc without rotation (AD), which only considers the axial force and typically uses the momentum theory (Rankine, 30 1865). These turbine wake models have been implemented in various Large Eddy Simulation (LES) models, including Ellip-Sys3D (AL) (Göçmen et al., 2016), MITRAS (AD+R) (Salim et al., 2018), Simulator for Wind Farm Applications (SOWFA) (AL) (Fleming et al., 2014; Churchfield et al., 2016), and the Parallelized Large-eddy Simulation Model (PALM) (AL, AD, AD+R) (Witha et al., 2014; Maronga et al., 2015, 2020). For applications where detailed near-wake structures are not essential, 35 AD+R and AD methods are preferred due to their lower computational cost, easier implementation, and sufficient accuracy for far-wake information (Breton et al., 2017).

Besides the accuracy of the turbine wake methods, a realistic ABL plays a crucial role in wake simulations. The processes that affect wind farms range from macro- and mesoscale weather phenomena down to the micro-scale of turbulence in the ABL (Porté-Agel et al., 2020). Given this multi-scale nature, a meso-to-micro numerical downscaling could be useful in 40 simulating the ABL-turbine interaction realistically and understanding its underlying mechanisms (Muñoz-Esparza et al., 2014; Bakhoday-Paskyabi et al., 2022a). To incorporate realistic ABL conditions, one can use the meso-micro offline coupling approach, i.e. the output of a mesoscale model is used as the driven boundary condition for the dedicated LES models (e.g. Wang et al., 2020; Lin et al., 2021; Bakhoday-Paskyabi et al., 2022b; Onel and Tuncer, 2023). However, this approach depends on the frequency of the mesoscale model output, which is often not enough for short time-scale processes. The second approach, 45 online coupling, uses a meso-micro coupled model system, where a mesoscale model and an LES model are coupled through a coupling interface. While the online coupling approach provides a seamless downscaling, it is more difficult to implement than the offline approach. The third approach, nested downscaling, involves a single model that can handle the downscaling naturally through a system of nested domains where the inner domains can be configured to run in LES mode. For example, the Consortium for Small-scale Modeling (COSMO) model (Baldauf et al., 2011) and the Weather Research and Forecast (WRF) model (Skamarock et al., 2019) provide this capability.

50 The WRF model is open-source software that is highly popular in the atmospheric research community for studying a wide range of atmospheric processes, from idealized studies to real-world applications. It facilitates a meso-to-micro nested downscaling framework capable of simulating turbine wakes under realistic Atmospheric Boundary Layer (ABL) conditions (Muñoz-Esparza et al., 2014; Bakhoday-Paskyabi et al., 2022a; Ning et al., 2023). Several WRF implementations include the effects of wind farms and wind turbines (e.g., Fitch et al., 2012; Volker et al., 2015; Mirocha et al., 2014; Kale et al., 2022), 55 which can be grouped into wind farm parameterization (WFP) and wind turbine model (WTM).

The WFP approaches (Fitch et al., 2012; Volker et al., 2015) are commonly used to study the collective effects of wind turbine wakes on the ABL and the interactions between wind farms (e.g. Pryor et al., 2020; Fischereit et al., 2022). One advantage

of these approaches is their low computational cost and ease of implementation. For example, the method used by Fitch et al. (2012) only requires the thrust and power curve data from turbine manufacturers. However, due to the limitation of the target 60 horizontal resolutions, which must be at least 3 to 5 rotor diameters (Fischereit et al., 2022), the WFP cannot explicitly resolve individual turbine wakes or turbine-to-turbine interactions. This may result in inaccurate evaluations of wakes behind wind farms (Lee and Lundquist, 2017). On the other hand, the implemented general actuator disc (GAD) model in WRF (Mirocha et al., 2014; Kale et al., 2022) employs the AD+R method based on the BEM theory. However, the GAD model requires more information about the turbine, such as blade profiles and aerodynamic characteristics as well as generator speed and blade 65 pitch control, which may sometimes be confidential and not publicly available. Further, the WRF-GAD implementation's source code has not been released publicly, limiting its use for the scientific community, despite the WRF being open-source.

To address these limitations, this study introduces a new wind turbine wake model named the Simple Actuator Disc for Large Eddy Simulation (SADLES) within the WRF framework. Unlike WRF-GAD, WRF-SADLES utilizes the traditional momentum theory that requires only basic information about the turbines, such as their thrust and power curves, similar to the 70 WFP model by Fitch et al. (2012). However, in contrast to Fitch et al. (2012), WRF-SADLES is capable of explicitly resolving turbine wakes similar to WRF-GAD. While many WRF-GAD applications typically employ fine resolutions of a few meters (e.g. Mirocha et al., 2014; Arthur et al., 2020; Kale et al., 2022), such high resolutions are computationally expensive for 75 realistic downscaling problems involving large domains with multiple wind farms. Therefore, WRF-SADLES is also tested with coarser resolutions (specifically, 30 and 40 meters) to achieve a more practical balance between computational cost and wake resolution. To facilitate its application within the meso-to-micro downscaling approach, we have also implemented the cell perturbation method (Muñoz-Esparza et al., 2014), which allows faster development of turbulence within nested domains. The WRF-SADLES code package is an open-source software suite encompassing both the SADLES module and the cell 80 perturbation module. Its development aims to be eventually integrated into the official WRF repository, fostering further open research within the weather forecasting community.

80 To validate the WRF-SADLES model, firstly, an idealized case is used to compare the simulations of a 5-MW wind turbine from WRF-SADLES with the PALM model. The reason for selecting PALM was that it includes a wind turbine model that uses the AD+R method based on the BE theory (Dörenkämper et al., 2015), which is comparable with the WRF-GAD model. Moreover, the PALM model has been shown to agree well with more sophisticated wake models and observations (Witha et al., 2014; Vollmer et al., 2015; Dörenkämper et al., 2015; Bakhoday-Paskyabi et al., 2022a, b). In addition, we demonstrated a more 85 realistic application of the WRF-SADLES by downscaling the ERA5 reanalysis data (Hersbach et al., 2020) to a 40-meter resolution around the Alpha Ventus wind parks, enabling us to investigate the effects of turbine-to-turbine and farm-to-farm interactions. The simulations are then compared with the observational data recorded at the FINO1 offshore meteorological mast station.

The rest of this paper is structured as follows. Section 2 details the WRF-SADLES method and implementation. Section 3 90 presents an idealized single-turbine simulation compared with the PALM model. Section 4 showcases a multi-scale downscaling application with multiple wind farm simulations. Section 5 concludes by summarizing the key findings and discussing the potential applications and limitations of the WRF-SADLES model.

## 2 Methods

### 2.1 The simple actuator disc for large eddy simulation

95 The actuator disc (Anderson, 2020) is a hypothetical surface perpendicular to the wind flow that extracts energy continuously from the ambient wind through the work of the thrust force:

$$\mathbf{F}_T = -\frac{1}{2}\rho C_T |\mathbf{V}_0| \mathbf{V}_0 A, \quad (1)$$

where  $\rho$  is the air density,  $A$  is the rotor area,  $C_T$  is the thrust coefficient, which is a function of the ambient (unperturbed) wind speed  $|\mathbf{V}_0| = \sqrt{u_0^2 + v_0^2}$ .

100 The tendency terms of the thrust force are incorporated into the WRF model at the grid cells where the actuator disc intersects:

$$\frac{\partial u}{\partial t} \Big|_T = -\frac{1}{2} C_T |\mathbf{V}_0| u_0 \frac{\delta A}{\Delta x \Delta y \Delta z}, \quad (2)$$

$$\frac{\partial v}{\partial t} \Big|_T = -\frac{1}{2} C_T |\mathbf{V}_0| v_0 \frac{\delta A}{\Delta x \Delta y \Delta z}, \quad (3)$$

where  $\delta A$  is the portion of the actuator disc area within the grid cell,  $\Delta x$ ,  $\Delta y$ , and  $\Delta z$  are the grid sizes. We can shorten the 105 formula by defining the area factor  $F_A = \delta A / (\Delta x \Delta y \Delta z)$ , which can be determined by performing a vertical and horizontal discretization of the actuator disc area (Fig. 1).

Normally, the unperturbed wind  $V_0$  is unknown, but is related to the wind speed at the rotor,  $\mathbf{V}$ , by:

$$\mathbf{V}_0 = \frac{1}{1-a} \mathbf{V}, \quad (4)$$

where  $a$  the axial induction factor. We note that in the WRF model, the tendency terms are defined for the coupled velocity, 110 which is defined as  $U = \mu_d u$ , with  $\mu_d$  as the dry mass of the air column. Thus the tendency terms to be added to the model become:

$$\frac{\partial U}{\partial t} \Big|_T = -\frac{1}{2(1-a)^2} \mu_d C_T |\mathbf{V}| u F_A, \quad (5)$$

$$\frac{\partial V}{\partial t} \Big|_T = -\frac{1}{2(1-a)^2} \mu_d C_T |\mathbf{V}| v F_A. \quad (6)$$

The turbulence in the wake behind a wind turbine primarily arises from shear due to reduced wind speed in the wake region 115 (Crespo et al., 1996; Quarton and Ainslie, 1990). In mesoscale modeling, incorporating turbulence kinetic energy (TKE) into wind farm parameterization is necessary due to the model's inability to resolve wakes at small scales (Fitch et al., 2012). Fitch

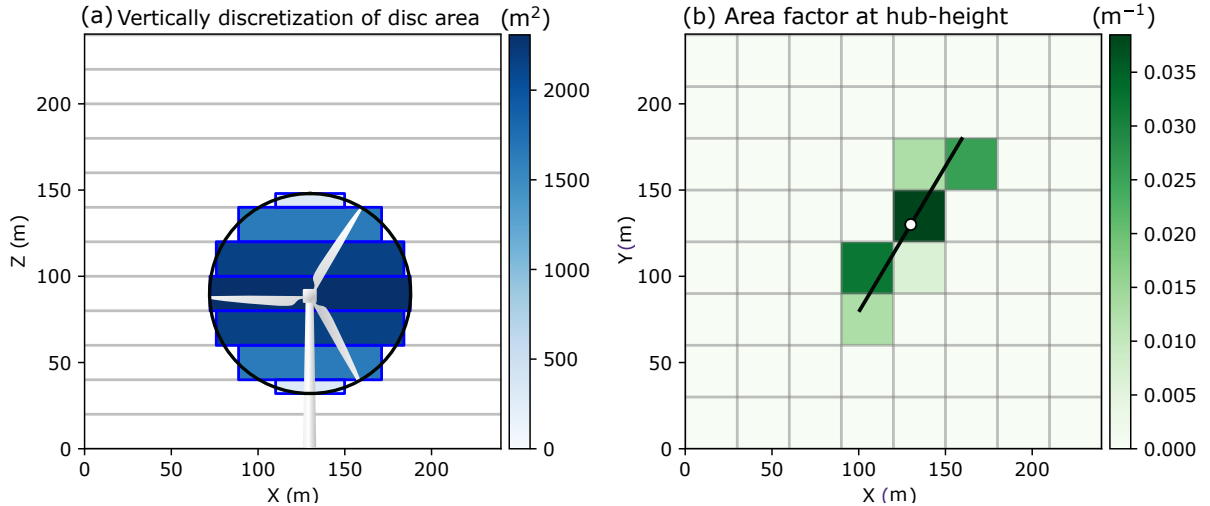


**Figure 1.** The illustration demonstrates the discretization of an actuator disc. (a) Vertically, the disc is divided into sections between each full vertical level. (b) The discretized area factor at the hub-height level is depicted. The actuation disc radius is 116 meters and the horizontal and vertical grid sizes are 30 meters and 20 meters, respectively.

et al. (2012) assumes that a portion of the extracted energy from the mean wind becomes power (related to power coefficient  $C_P$ ), while the remainder becomes TKE, proportional to  $C_T - C_P$ . Given WRF-SADLES's target resolution of a few dozen meters, where the wake is partially resolved, some added subgrid-scale TKE may be necessary. Nevertheless, we tested the 120 method used by Fitch et al. (2012), incorporating a source of subgrid-scale TKE as:

$$\frac{\partial TKE_{sgs}}{\partial t} \Big|_T = \frac{1}{2(1-a)^3} \mu_d C_{TKE} |\mathbf{V}|^3 F_A \quad (7)$$

where  $C_{TKE} = f_{TKE}(C_T - C_P)$ , with  $f_{TKE}$  is a factor that controls the amount of kinetic energy loss converted to TKE.

The tendency terms above depend critically on the axial induction factor  $a$ . Some previous studies have used certain specific values of  $a$ , such as  $a = 1/4$  (Calaf et al., 2010) or even  $a = 0$  (Fitch et al., 2012) (i.e. they used the wind speed at the grid point 125 directly instead of the unperturbed wind speed). In our implemented SADLES model, we provide two options for estimating  $a$ :

- Option 1 (direct evaluation): First, the hub-height ambient wind speed  $|\mathbf{V}_0|$  is evaluated at two rotor diameters ( $2D$ ) in front of the turbine. Then, the induction factor is calculated by:

$$a = 1 - \frac{|\mathbf{V}|}{|\mathbf{V}_0|},$$

- 130
  - Option 2 (inferred evaluation): In this option, only the hub-height wind speed at the rotor location is needed. Instead, we assume the 1-dimensional momentum theory ( $C_T = 4a(1-a)$ ) and therefore:

$$a = \frac{1}{2}(1 - \sqrt{1 - C_T(|\mathbf{V}|)}).$$

135 Note that although the thrust curve is typically provided as a relation between  $C_T$  and the ambient wind speed  $|\mathbf{V}_0|$ , we can also establish the relation between  $C_T$  and the wind speed at the rotor  $|\mathbf{V}|$  using the 1-dimensional momentum theory.

In general, the direct evaluation of  $a$  (Option 1) is more intuitive. However, this method has some potential problems, including the formula being affected by the blockage effect, where the wind speed in front of the wind turbine is reduced. By using this formula,  $a$  can exceed 0.5, implying that the wind behind the turbine becomes opposite to the ambient wind. This is nonphysical and can lead to model instability. Thus, the upper limit of  $a$  is set to its inferred evaluated value (Option 2).

## 140 2.2 Cell perturbation

Traditional LES simulations often use periodic lateral boundary conditions, allowing turbulent eddies to fully develop and reach a quasi-steady state. However, nested downscaling approaches face limitations due to the restricted time and space within the inner domain. This restricted environment can hinder the complete development of eddies, particularly in scenarios with small domain sizes, high ambient wind speeds, or stable boundary layer conditions. These limitations can lead to slow turbulence 145 development within the nested domain, impacting the accuracy of simulations.

The above problem can be alleviated using the cell perturbation method (Muñoz-Esparza et al., 2014, 2015), which is a simple and effective way to accelerate the development of turbulence within the nested domain. The method introduces a random perturbation of potential temperature within the interval of -0.5K to 0.5K to three cells near the inflow boundaries. Each cell is an 8x8 grid points square in the horizontal plane, and the same perturbation is applied to each cell. Therefore, the 150 total perturbation zone extends 24 grid points from the inflow boundaries.

In the idealized setup of Muñoz-Esparza et al. (2014), perturbations are introduced at every vertical grid point up to two-thirds of the inversion layer, which is known in the idealized setting. In our approach, the perturbations are applied with full magnitude up to a pre-defined vertical level  $k_1$  and then gradually reduced to zero at a higher level  $k_2$  using the weight  $\cos^2[0.5\pi(k - k_1)/(k_2 - k_1)]$ , where  $k$  is the vertical level. As noted by Muñoz-Esparza et al. (2014), the perturbation process 155 should not be done at every time step, but at an interval that is at least equal to the perturbation time scale,  $T_s = 8\Delta x/U$ , where  $U$  is the characteristic velocity scale and  $\Delta x$  is the horizontal grid spacing.

Because the cell perturbation method is not available with the distribution of WRF, we included our implementation within the distribution of WRF-SADLES.

## 2.3 Code implementation and turbine information

160 We've integrated the SADLES code into the Advanced Research WRF (ARW), version 4.3.1, with MPI support. This was achieved by adding two new Fortran 90 modules: a SADLES module (*module\_sadles.F*) and a cell perturbation module (*module\_cellpert.F*), both serve as the WRF's physics package (located in the *phys* directory). The new namelist options for these modules were incorporated into the WRF model by modifying the WRF's Registry. During the first step of the Runge-Kutta

loop (within *module\_first\_rk\_step\_part1.F*), tendency terms of the SADLES module are added to the model, while the potential 165 temperature perturbation from the cell perturbation is incorporated after the integration loop (within *solve\_em.F*).

Tables A1 and A2 outline the available options in the SADLES and cell perturbation modules. This modified WRF system also enables the simulation of turbine behavior in idealized experiments, with additional namelist options for specifying the Coriolis parameter and surface roughness length. The code has been released as open-source to foster open research (Bui, 2023), with the aspiration of its inclusion in the official WRF repository. Users can implement the WRF-SADLES by copying 170 these modules and overriding a few related files within the existing WRF file structure, followed by recompiling the model system. In the subsequent section, we utilize turbine data from Larsén and Fischereit (2021), which provides the locations, thrust curves, and power curves of wind turbines from various wind farms in the North Sea.

### 3 Idealized simulation

#### 3.1 Experiment design

175 To start, we investigate the calculation of the axial induction factor (e.g., Option 1 or Option 2) and the additional tendency for sub-grid TKE (i.e.,  $f_{TKE}$ ). Due to challenges in acquiring relevant observational data, we conducted and compared idealized experiments employing a single 5-MW turbine using the WRF-SADLES and PALM models. Simulations were executed at two resolutions: 10 meters (high resolution, about 12 grid points per rotor diameter) and 30 meters (target intermediate resolution, about 4 grid points per rotor diameter).

180 Table 1 summarizes the experiments conducted using the WRF-SADLES and PALM models. For the WRF-SADLES simulations, experiments with suffixes \_Opt1 and \_Opt2 represent different options for calculating the axial induction factor  $a$ , with Option 1 employing direct evaluation and Option 2 employing inferred evaluation. In these experiments,  $f_{TKE}$  takes the default value of 0.5. Additionally, experiments with suffixes \_TK0 and \_TKE1, both utilizing Option 2, aim to investigate the effect of adding TKE tendency as in Equation (7), with  $f_{TKE}$  set to 0 and 1, respectively.

#### 185 WRF-SADLES configurations

The domain configurations for each experiment are summarized in Table 1. Each experiment utilized two nested domains (D01 and D02), with the outer domain D01 having a coarser resolution (30 meters or 90 meters) and using periodic boundary conditions on all sides, and the inner domain D02 (10 meters or 30 meters) applying cell perturbation at the inflow boundary on the west side. All domains except the 10-meter domain had a horizontal aspect ratio of 2:1. The 10-meter domain had a 190 longer aspect ratio of 2.76:1 to allow the turbulence and turbine wake to evolve over a longer distance.

The top model level for all experiments is set at 1600 meters, with an 800-meter Rayleigh damping layer at the top with a coefficient of  $0.2 \text{ s}^{-1}$ . There is no vertical level stretching for the 30-meter resolution experiments. In the case of the 10-meter experiments, the vertical levels are stretched such that the near-surface vertical resolution is roughly 10 m. The initial potential temperature is 288 K from the surface up to 500 m, and then increases with a lapse rate of 1 K/100 m.

**Table 1.** Domain configurations for the idealized WRF (prefix W) and PALM (prefix P) experiments

Experiments	Domain	$N_x \times N_y \times N_z$	$\Delta x [m]$	$\Delta t [s]$	$L_x [m]$	$L_y [m]$
W30m_Opt1, W30m_Opt2,	D01	$322 \times 163 \times 91$	90	1/2	28890	14490
W30m_TKE0, W30m_TKE1	D02	$322 \times 163 \times 91$	30	1/6	9660	4860
W10m_Opt1, W10m_Opt2,	D01	$322 \times 163 \times 91$	30	3/20	9660	4860
W10m_TKE0, W10m_TKE1	D02	$448 \times 163 \times 91$	10	1/20	4470	1620
P30m	D01	$336 \times 172 \times 90$	90	1/2	30240	15480
	D02	$336 \times 192 \times 160$	30	1/6	10080	5760
P10m	D01	$336 \times 176 \times 160$	30	3/20	10080	5280
	D02	$432 \times 192 \times 150$	10	1/20	4320	1920

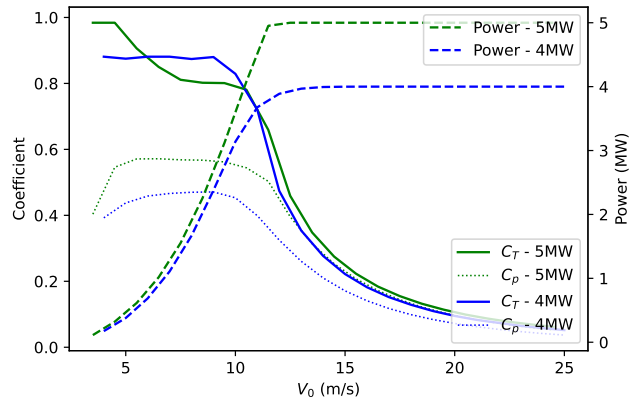


**Figure 2.** Thrust coefficient ( $C_T$ ), power coefficient ( $C_P$ ), and turbine power as functions of ambient wind speed ( $V_0$ ) are shown for the 4 MW and 5 MW wind turbines used in the idealized (5 MW) and realistic (4 MW and 5 MW) experiments in this paper.

195 Our idealized simulations employed the Revised MM5 Monin-Obukhov surface layer scheme (Jiménez et al., 2012) with a surface roughness length of 1 mm. We enabled LES mode by deactivating the boundary layer parameterization scheme. Instead, the 1.5-order three-dimensional TKE closure was used (Lilly, 1967), treating the subgrid-scale TKE as a prognostic variable. The Coriolis parameter was set to  $1.177 \times 10^{-4} \text{ s}^{-1}$ , corresponding to a 54°N latitude.

200 In idealized LES, the focus is on resolving the turbulent structures within the domain. To achieve this, non-essential physical parameterization schemes, including microphysics, cumulus convection, and radiation, were disabled. The effect of surface radiation on the development of turbulence is represented by a surface turbulence heat flux of  $\overline{(\theta'w')}_s = 0.02 \text{ K m s}^{-1}$ , similar to some previous studies (Muñoz-Esparza et al., 2014; Kale et al., 2022). This presents a weak convective boundary layer.

205 At the center of the inner domain, we placed a 5 MW wind turbine used at the Alpha Ventus wind farm. The turbine information taken from Larsén and Fischereit (2021) includes a rotor diameter of 116 m, a hub height of 90 m, and the thrust and power curves at different wind speeds (Fig. 2).

210 To achieve a quasi-equilibrium state of turbulence, a specialized LES model such as PALM typically conducts a precursor run, often using a smaller domain to minimize computational costs. However, this precursor technique is not supported within the WRF model. Instead, we opt for a spin-up period of 20 hours solely in the outer domain. To align the wind within the boundary layer predominantly in the zonal (eastward) direction, we adjust the geostrophic wind to rotate slightly to the left, specifically setting  $U_g = 10.24 \text{ m/s}$  and  $V_g = -1.39 \text{ m/s}$ . Following the spin-up period, both domains are simulated for 4 hours, with a 1-minute output interval for the inner domain (D02) to facilitate further analysis.

## PALM configurations

215 To evaluate the performance of the SADLES module in simulating turbine wakes, we compared the results from the WRF-SADLES model with those from the PALM model, (Maronga et al., 2015, 2020), system 21.10 revision r4901. PALM is an LES model developed at Leibniz Universität Hannover, Germany, and has been shown in several studies to be capable of simulating wind turbine wakes effectively (e.g. Witha et al., 2014; Vollmer et al., 2015; Dörenkämper et al., 2015).

220 In PALM, the wind turbine is represented by an advanced AD+R model that is based on the BE method (Dörenkämper et al., 2015), which calculates both the thrust and torque forces as functions of radius and tangential angle from the center of the rotor. Similar to the GAD methods (Mirocha et al., 2014; Kale et al., 2022), the wind turbine model in PALM computes the local lift and drag forces and requires additional information on the turbine and blade aerodynamic properties. For this reason, currently only three types of wind turbines are officially supported, including the National Renewable Energy Laboratory (NREL) 2.3-MW, 5-MW and 15-MW models (Jonkman et al., 2009; Gaertner et al., 2020; Ardillon et al., 2023). To compare with WRF-SADLES, we used the NREL 5-MW model with the same hub height of 90 m. However, the rotor diameter of the NREL 5-MW is slightly larger at 128 meters compared to the 116-meter diameter of the 5-MW turbine used in WRF-SADLES.

225 The two idealized experiments, P10m and P30m, with two nested domains similar to the WRF-SADLES experiments (see Table 1 for domain configurations). Cyclic lateral boundary conditions were used for the coarser domain. To prepare initial conditions for the main run we used a precursor run for 24 hours to reach a quasi-steady state condition. Compared to the

simulation domain, the precursor domain has the same number of vertical levels, but has only  $96 \times 64$  horizontal grid points to reduce the computational cost.

230 To parameterize subgrid-scale turbulence in PALM, we used 1.5-order closure (Deardorff, 1980; Moeng and Wyngaard, 1988; Saiki et al., 2000). We initialized atmospheric conditions similar to those in the WRF-SADLES experiments, including an initial potential temperature of 288 K, a surface turbulence heat flux of  $\overline{(\theta'w')}_s = 0.02 \text{ W m s}^{-2}$ , and a geostrophic wind of approximately 10 m/s from the west.

### 3.2 Result

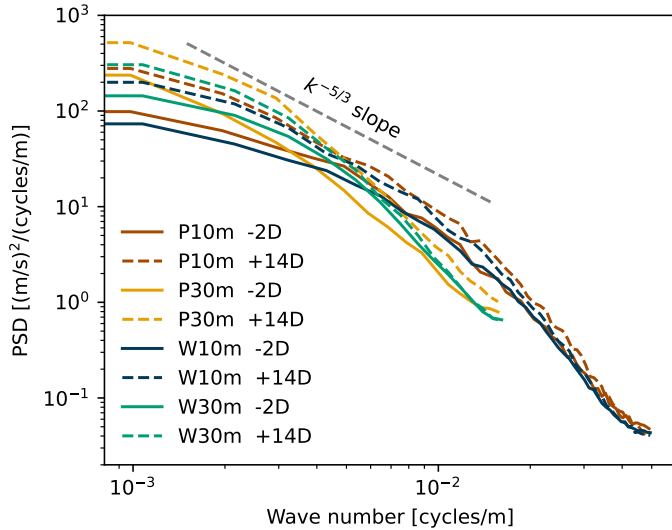


**Figure 3.** Time-averaged power spectral densities (PSDs) of wind speed spatial fluctuations for the PALM (P10m, P30m) and WRF-SADLES (W10m, W30m) simulations at two locations:  $-2D$  upstream and  $+14D$  downstream of the wind turbine. The analysis was computed from a meridional (south-north direction) line at hub height with a length of  $8D$  centered on the wake center. To improve clarity and avoid redundancy, we present the average results of all WRF-SADLES simulations at each resolution (W30m and W10m for 30-meter and 10-meter resolutions, respectively).

235 We first examine the turbulence characteristic of WRF-SADLES and PALM at different resolutions by carrying out wave-number spectra analysis for a meridional (south-north) cross-section at hub height with a length of  $8D$ , centered on the wake axis (Fig. 3). Both WRF-SADLES and PALM simulations exhibit similar trends in turbulence properties. Simulations with a 10-meter resolution capture higher turbulence levels for smaller-scale structures (wavenumbers  $> 4 \times 10^{-3}$  cycles/m, corresponding to wavelengths shorter than 250 meters). This indicates a better ability to resolve these structures with finer resolution. This  
240 suggests limitations in capturing the energy transfer mechanisms at these scales. Compared to the 30-meter resolution, the 10-meter resolution exhibits a broader range of applicability for the Kolmogorov power law, spanning from approximately  $2 \times 10^{-3}$  to  $10^{-3}$  cycles/m (corresponding to wavelengths between 100 meters and 500 meters). This wider range signifies a more

245 accurate representation of the energy cascade across different scales in these simulations. Furthermore, all simulations show an increase in turbulence energy at the far-wake distance ( $14D$ ) compared to upstream turbulence ( $-2D$ ), for all wavenumbers, indicating that the turbine has an effect of increasing the turbulence behind it. This behavior is consistent for both PALM and WRF-SADLES models.

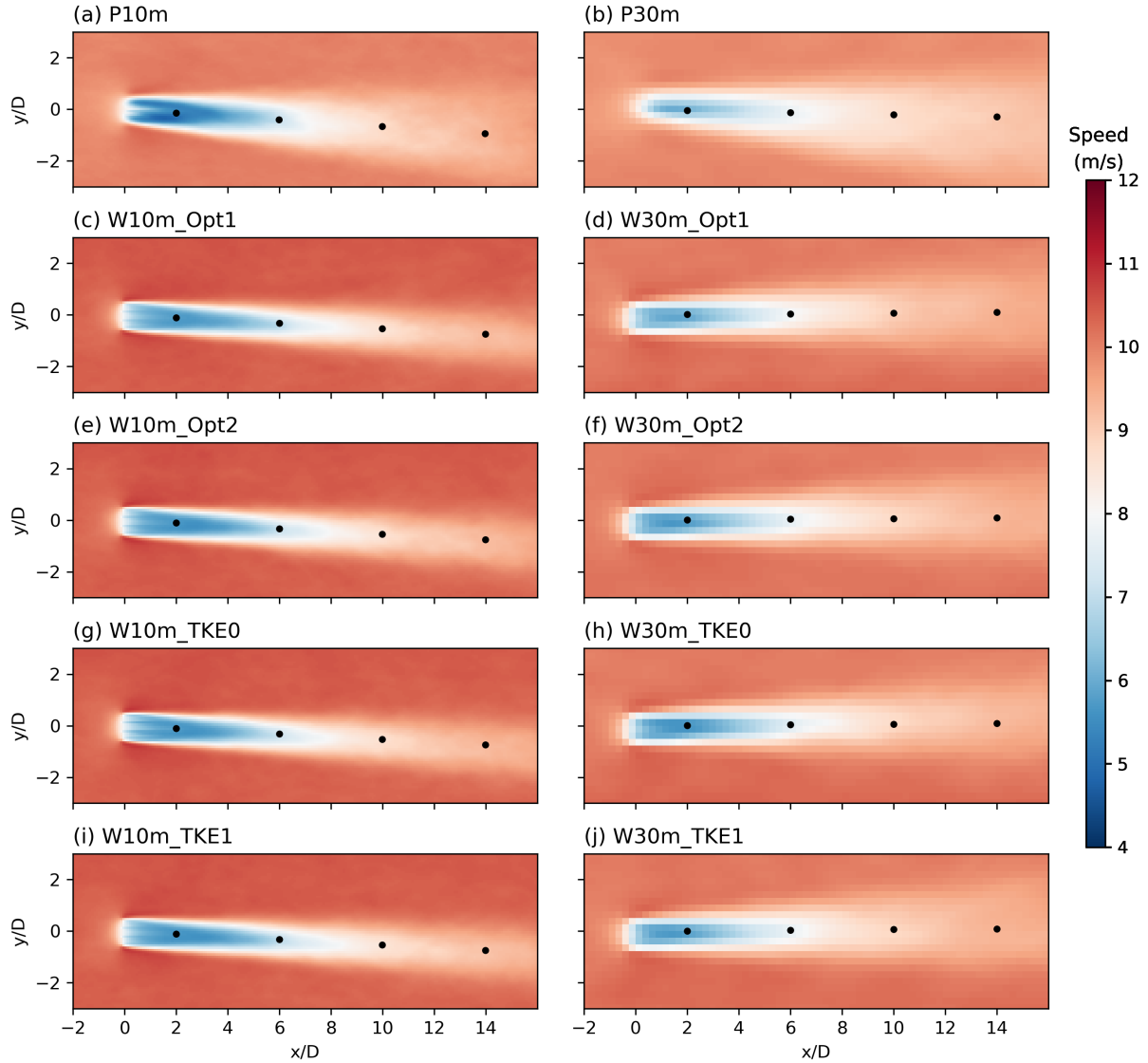


**Figure 4.** 4-hour average wind speeds at the turbine hub height (90 m) for PALM (a, b) and WRF-SADLES (c–j) simulations with different resolutions and options for axial induction factors and  $f_{TKE}$  values ( $=0$  for  $_TKE0$ ,  $=1$  for  $_TKE1$ ). Black dots indicate distances of  $2D$ ,  $6D$ ,  $10D$ , and  $14D$  behind the turbine.

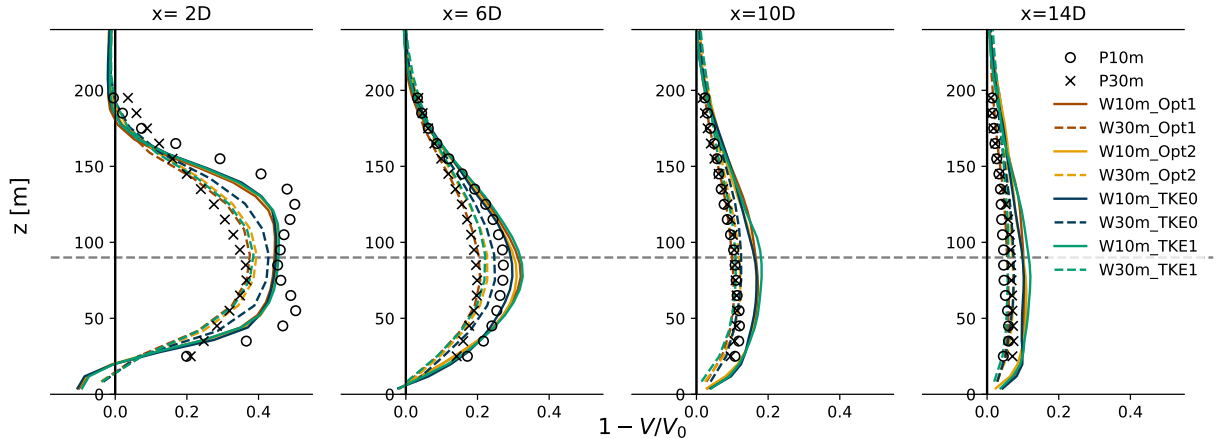


**Figure 5.** Vertical profile of wake deficit ( $1 - V/V_0$ ) for idealized experiments at distances behind the turbine of  $2D$ ,  $6D$ ,  $10D$ , and  $14D$ . The evaluation locations are indicated by black dots in Fig. 4.

Figure 4 shows the average wind speeds over 4 hours for the PALM and WRF-SADLES idealized experiments. For both PALM and WRF-SADLES, the differences between 10-meter and 30-meter resolution are more noticeable than the difference between the two models and between different options of WRF-SADLES. Vertically, the 10-meter resolution PALM exhibits two maximums above and below the hub height at the near wake distance (Fig. 5,  $x = 2D$ ) which results from the BE method. This feature is not present in the 30-meter PALM simulation and the WRF-SADLES experiments. For further distances downstream, there is a similarity in the shape of the wake deficit for 10-meter and 30-meter for both models with one single maximum slightly below the hub height (Fig. 5,  $x = 6D, 10D, 14D$ ).

Both PALM and WRF-SADLES simulations have a stronger wake deficit for higher resolution for distances shorter than  $6D$  (Fig. 5). For longer distances, the wake deficit of 10-meter PALM eventually becomes weaker than 30-meter, indicating a faster wake recovery and stronger turbulence activity for the higher resolution. On the contrary, the wake deficit of 10-meter WRF-SADLES at a longer distance of  $14D$  is still significantly stronger than the 10-meter simulation, indicating a slower wake recovery. Visibly, the 10-meter WRF-SADLES simulations exhibit weaker wake expansion than the 30-meter WRF-SADLES simulation, which is more in agreement with the 10-meter PALM simulation (Fig. 4).

Minimal differences are observed for the two methods calculating the axial induction factor in WRF-SADLES (Fig. 4 and Fig. 5). This validates the 1-D momentum theory of the actuator disc for calculating axial induction factor  $a$ . Given that Option 1 necessitates wind speed evaluation in front of the turbine, it may be sensitive to model resolution and blockage effects. Therefore, we recommend the use of Option 2 in practical applications. Additionally, being derived from the 1D momentum theory, Option 2 is also consistent with the simple actuator disk method of WRF-SADLES.

Compared to the two axial induction factor calculation methods within WRF-SADLES, the effects of subgrid-scale TKE are more pronounced on wake development (Fig. 5, at  $2D$  and  $6D$ ). Using the 10-meter PALM simulation as a reference, the WRF simulation without added TKE ( $f_{TKE} = 0$ ) exhibits the best agreement in terms of wake deficit for both 10-meter and

30-meter resolutions at all distances. At distances exceeding 10D, the 30-meter WRF-SADLES simulation even gets closer to the reference than the 10-meter WRF-SADLES. Interestingly, at the 10-meter resolution, WRF-SADLES with added TKE 270 (W10m\_TKE1) shows a slightly slower wake recovery compared to the experiment without added TKE (W10m\_TKE0), evident by a stronger wake deficit at 10D and 14D in Fig. 5.

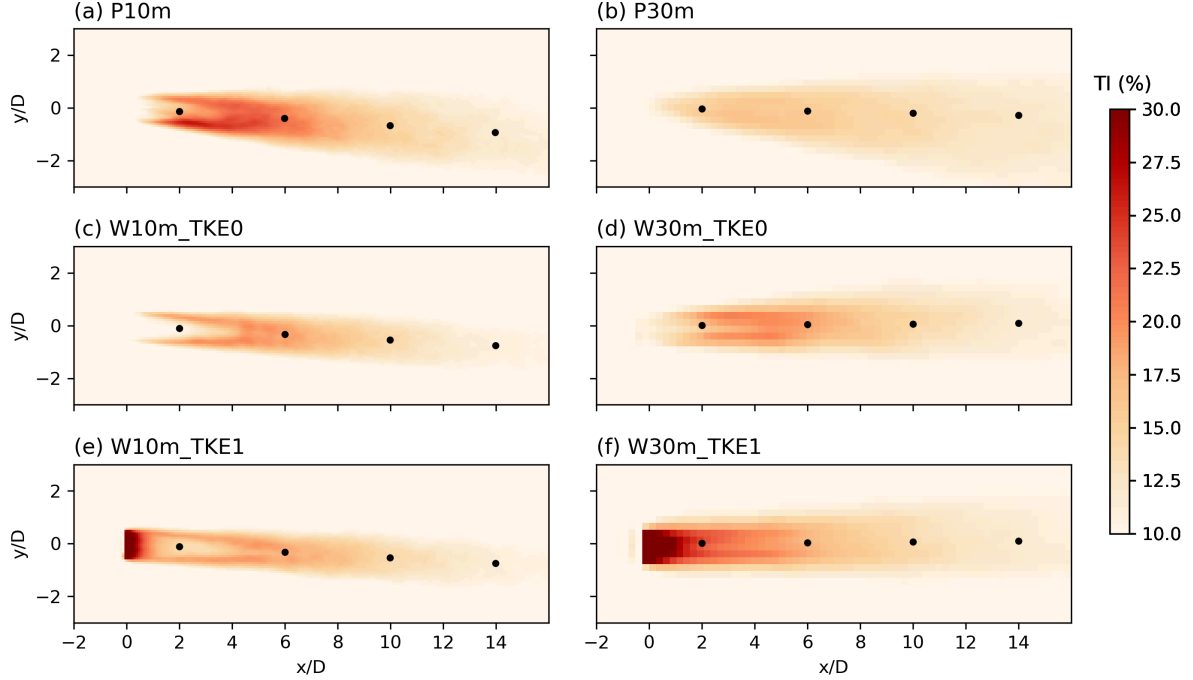


**Figure 6.** 4-hour turbulence intensity ( $\overline{TI}$ ) at hub height (90 m) for PALM (a, b) and WRF-SADLES (c–f) simulations with (\_TKE1), or without added TKE (\_TKE0) and different resolutions of 10 meters and 30 meters. Black dots indicate distances of 2D, 6D, 10D, and 14D behind the turbine.

To investigate why the added subgrid-scale TKE source has minimal impact on the wake development in WRF-SADLES, and even exhibits a negative impact on wake recovery at the 10-meter resolution, we compared the calculated average turbulence intensity (TI) between the experiments. The average TI is computed using the following equation:

$$275 \quad \overline{TI} = \frac{\sqrt{\frac{2}{3} \overline{TKE}}}{|\mathbf{V}|}, \quad (8)$$

where  $\overline{TKE}$  represents the time-averaged total turbulence kinetic energy, is the sum of gridscale ( $\overline{TKE}_{gs}$ ) and subgrid-scale ( $\overline{TKE}_{sgs}$ ) terms.  $\overline{TKE}_{sgs}$  is a prognostic variable derived from the 1.5-order turbulence closure within the PALM and WRF-SADLES models. On the other hand, the gridscale term is derived from  $\overline{TKE}_{gs} = \frac{1}{2}(u'^2 + v'^2 + w'^2)$ , where  $u', v', w'$  denote the deviations of wind speed components from their respective time averages over the simulation period.

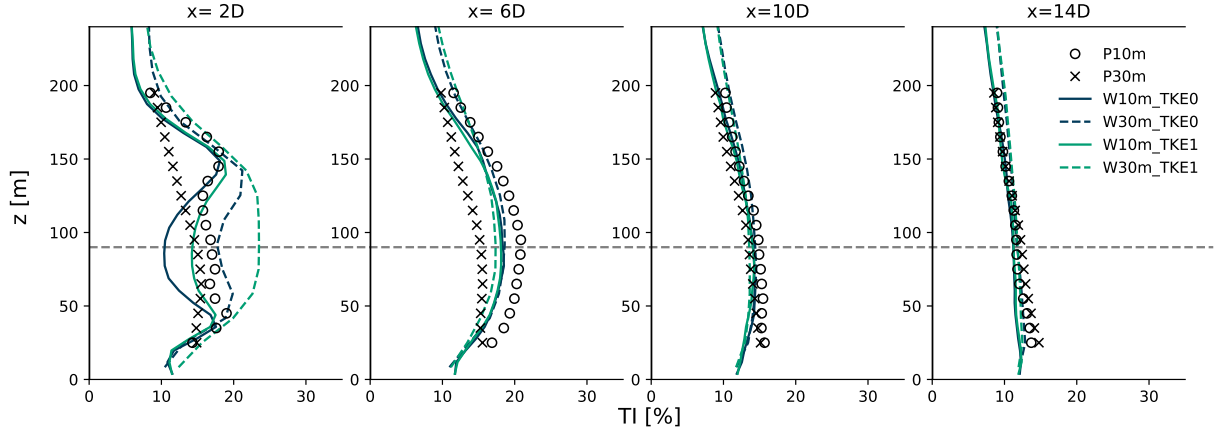


**Figure 7.** Vertical profile of time-averaged turbulence intensity  $\overline{TI}$  for PALM and WRF-SADLES simulations with (\_TKE1), or without added TKE (\_TKE0) at distances behind the turbine of  $2D$ ,  $6D$ ,  $10D$ , and  $14D$ . The evaluation locations are indicated by black dots in Fig. 4.

280 All experiments show a consistent TI of around 10% outside the wake regions (Figs. 6 and 7). Both PALM and WRF-  
 285 SADLES simulations exhibit TI development at the edges of the wake regions due to the increased wind shear at these boundaries (Fig. 6). Without added TKE, the TI at the turbine location is equal its the environmental value. When the subgrid-scale TKE is added (\_TKE1), the TI has a maximum TI exceeding 30% at the turbine location (Figs. 6e, f). Significant discrepancies in the TI profiles are observed only in the vertical profiles of TI between the two models (PALM and WRF-SADLES) and resolutions (10 meters and 30 meters) at the near-wake distance (Fig. 7,  $x = 2D$  ). The experiments with 10-meter resolution show two TI peaks above and below the hub height, likely due to the turbulence production associated with the wake shear. These peaks reach a TI of about 20% and are consistent between the PALM and WRF-SADLES models.

290 However, these added subgrid-scale TKE primarily impacts the near-wake region and has minimal effect further downstream (Fig. 7,  $x = 6D, 10D, 14D$ ) as the TI quickly dissipates as it advects downstream. The TI levels for WRF-SADLES without added TKE even show better agreement with the reference experiment for both resolutions (30-meter and 10-meter). These findings challenge the underlying assumption of Fitch et al. (2012), as the TKE downstream should relate to wake deficit, which is linked to  $C_T$ , not to  $C_T - C_P$ . In an idealized scenario where all TKE extracted from the mean wind converts to power ( $C_T = C_P$ ), according to Fitch, no TKE is generated, which is not appropriate. Thus, we propose that hat mesoscale WFPs should consider the relationship between added turbulence and  $C_T$ , alongside factors like stability conditions. Therefore, 295 we recommend using the WRF-SADLES model without the added subgrid-scale TKE source (i.e.,  $f_{TKE} = 0$ ) in practical applications.

## 4 Meso-to-micro realistic downscaling simulation

This section demonstrates meso-to-micro downscaling using global reanalysis data. We employ the ERA5 data set from the European Centre for Medium-Range Weather Forecasts (ECMWF) (Hersbach et al., 2020). This data has a spatial resolution of approximately 31 kilometers and is available hourly. First, we briefly compare the simulation results with observational data from the FINO1 meteorological station in the southern North Sea. This comparison aims to assess the model's ability to reproduce real-world conditions. Subsequently, we will provide an example illustrating power loss due to farm-to-farm interaction.

### 4.1 Model configurations

To achieve turbine-scale resolution, we employed a system of five nested domains (detailed in Table 2). Each domain progressively reduces its grid size for finer resolution. The first three domains (D01, D02, D03; see Fig. 8a) focus on downscaling the mesoscale processes, while the final two domains (D04, D05; see Fig. 8b) transition to Large Eddy Simulation (LES) for high-resolution wind flow near the turbines.

The outermost domain (D01) has a resolution of 9 kilometers, encompassing a vast region that includes Europe and the North-East Atlantic Ocean (Figure 8a). The second domain (D02) zooms in on the North Sea (Figure 8a). The remaining three domains are centered around the Alpha Ventus wind farm, located near the FINO1 meteorological mast station (Figure 8b).

The first LES domain (D04) has a resolution of 200 meters and acts as an intermediate step between the meso-scale and turbine-scale domains. It does not include wind turbines within its simulation. The innermost domain (D05) has the highest resolution of 40 meters and encompasses a smaller area ( $19.2 \text{ km} \times 19.2 \text{ km}$ ) compared to a single grid cell of the original ERA5 data. This is the domain where the SADLES model is activated for simulating turbine wakes.

In domain D05, four wind farms are present comprising 5-MW and 4-MW turbines. Notably, the Alpha Ventus wind farm, featuring twelve turbines, is situated to the right of the FINO1 mast station. Detailed turbine specifications, including power and thrust curves, can be referenced in Larsén and Fischereit (2021) (refer to Fig. 2). For the subsequent experiments, we adopted the SADLES Option 2 for the inferred evaluation of the axial induction factor, along with the  $f_{TKE}$  value of 0.

For vertical grid resolution, we adopted 60 levels following Bui and Bakhoday-Paskyabi (2022). This setup provides high resolution near the surface, approximately 10 meters, with 21 levels below 500 meters height. Regarding physical parameterization, we employed the following options: the RRTMG (Rapid Radiative Transfer Model for General Circulation Models) scheme (Iacono et al., 2008) for radiation parameterization across all domains, the Thompson graupel scheme (Thompson et al., 2008) for microphysics parameterization. The Tiedtke scheme (Zhang et al., 2011) was utilized for cumulus parameterization in the outermost 9-km domain (D01), with cumulus parameterization disabled in finer resolution domains. For surface layer parameterization, we utilized the Monin-Obukhov Similarity scheme (Jiménez et al., 2012), and the Noah Land Surface Model (Mukul Tewari et al., 2004) was employed for land surface parameterization in all domains. The Yonsei University (YSU) scheme (Hong et al., 2006) was chosen for PBL parameterization in mesoscale domains (D01-D03), while PBL parameterization was disabled in LES (Large Eddy Simulation) domains (D04, D05). To simulate large eddies in LES domains,

**Table 2.** WRF domain configurations for the realistic downscaling experiments.

Domain	$N_x \times N_y \times N_z$	$\Delta x$ (m)	$\Delta t$ [s]	$L_x$ [km]	$L_y$ [km]
D01	$385 \times 321 \times 60$	9000	45	3456	2880
D02	$481 \times 382 \times 60$	3000	15	1440	1143
D03	$322 \times 322 \times 60$	1000	5	321	321
D04	$321 \times 321 \times 60$	200	1	64	64
D05	$481 \times 481 \times 60$	40	1/5	19.2	19.2

330 we employed the 1.5-order three-dimensional TKE closure (Lilly, 1967), supplemented by the cell perturbation method along the southern and western boundaries for the first 16 levels from the surface (up to approximately 300-meter height) to initiate turbulence development.

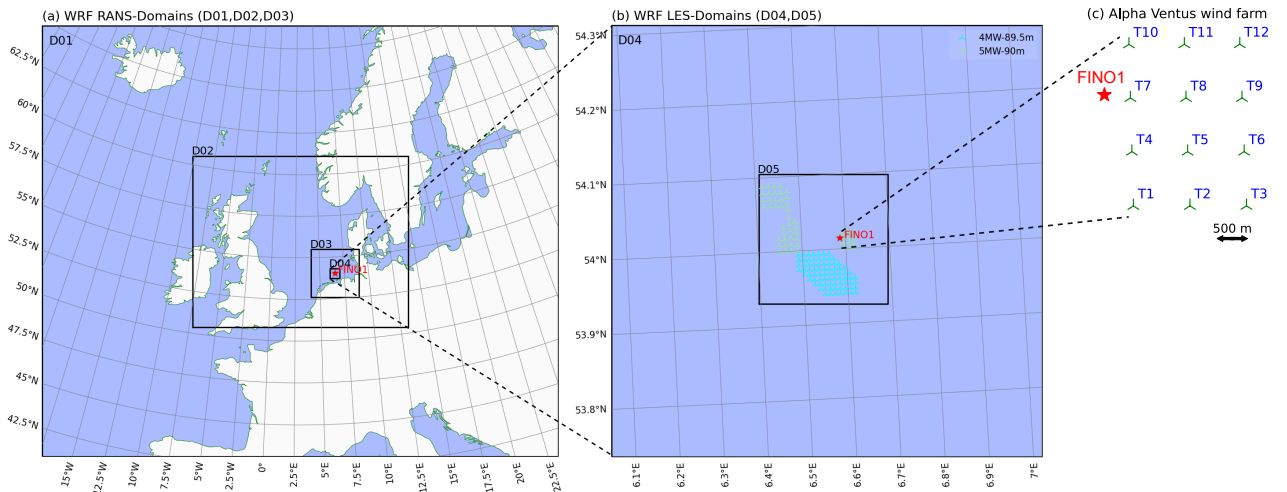


**Figure 8.** WRF domains used in the meso-to-micro downscaling simulations. The first three domains (a, D01-D03) are for mesoscale simulations, while the two innermost domains (b, D04, D05) are for LES simulations. The SADLES model is enabled in D05, with wind turbine locations marked by green and cyan markers. (c) Layout of the 12-turbine Alpha Ventus wind farm. The FINO1 meteorological mast station is indicated by the red star. Refer to Table 2 for detailed domain dimensions.

## 4.2 Comparison with observational data

This section briefly evaluates the performance of WRF-SADLES using observations from the FINO1 meteorological mast station. We compare wind speed and direction data collected by cup anemometers at 90 meters (hereafter referred to as "mast data") with WRF-SADLES simulations. Additionally, we utilize data from a Windcube® 100s wind LiDAR (Kumer et al.,

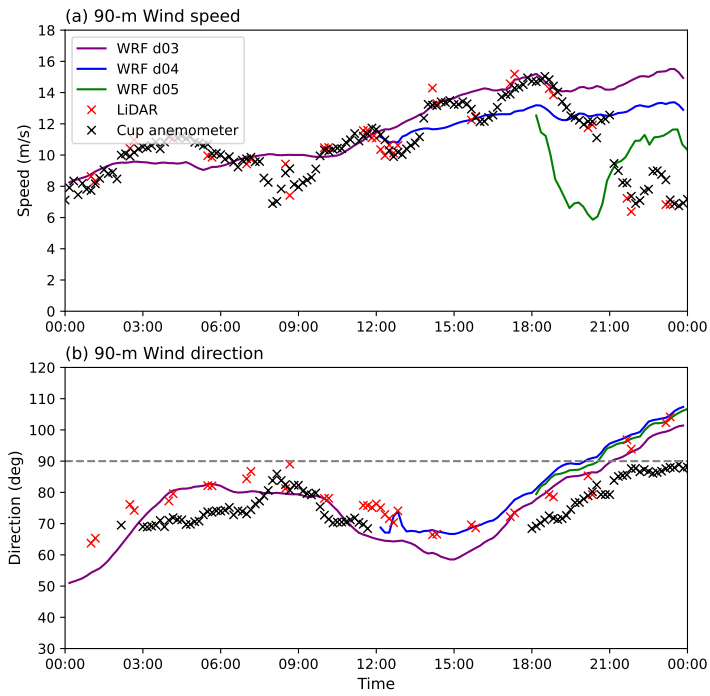


**Figure 9.** Time series of hub-height wind speed (a) and wind direction (b) at the FINO1 met-mast station on August 13, 2015, from 00:00 to 24:00 UTC, data from WRF-meso (d01), WRF-LES (d02), WRF-SADLES (d03), LiDAR, and cup anemometers (Mast).

2014) (hereafter referred to as "LiDAR data"). The LiDAR data provides vertical profiles of wind speed and direction from vertical scans, along with line-of-sight (LOS) velocity from horizontal scans.

The simulation period spans from 00:00 to 24:00 UTC on August 12, 2015. During this time frame, the first three domains (D01, D02, D03) run from 00:00 to establish mesoscale conditions, while the 200-meter WRF-LES domain (D04) begins at 12:00 UTC to serve as an intermediary between meso- and micro-scales. Finally, the 40-meter WRF-SADLES domain starts at 18:00 UTC to simulate turbine wakes. This period was selected because, towards its end, the wind direction shifts eastward, allowing for observation of wake effects using measurement data from the Fino1 station. Additionally, a low-level jet (LLJ), characterized by maximum wind speeds within the atmospheric boundary layer (ABL), is also observed during this timeframe.

Figure 9 compares wind speed and wind direction at 90 meters (hub height of the 5-MW Alpha Ventus wind turbines) from WRF simulations (D03: WRF-meso, D04: WRF-LES, and D05: WRF-SADLES) with observations from the FINO1 mast. Observations from both the mast data and LiDAR data suggest the wake effect from nearby turbines partially reduces wind speeds around 9:00, 13:00, 17:00, and 19:00 UTC, with reductions of approximately 2 m/s. From 22:00 onwards, the wakes exhibit a full effect, particularly when the wind direction approaches easterly (90 degrees), with wind speeds reduced from 6

350 to 8 m/s. While both data sources show good agreement in wind speed, there is a consistent difference of around 10 degrees in wind direction between the mast data and LiDAR data.

After a few hours of spin-up time, WRF-meso wind speeds agree well with observations when wakes do not affect the location. However, the intermediate LES domain (D05) underestimates wind speeds by about 2 m/s. Without the inclusion 355 of the wind turbine model, neither WRF-meso nor WRF-LES captures the wake effect at the FINO1 location. In contrast, WRF-SADLES, which includes a wind turbine model, successfully simulates the full wake effect at FINO1. Wind speeds are reduced to around 6 m/s, aligning well with observations. However, the timing of the wake impact differs, occurring between 19:00 and 21:00 UTC, roughly 2 hours earlier than observed.

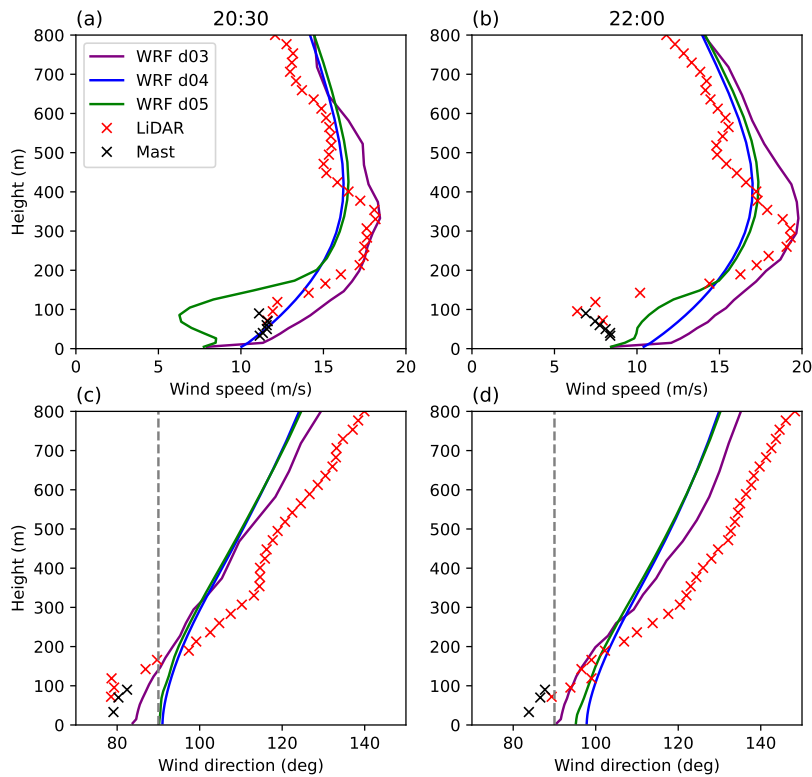


**Figure 10.** Vertical profiles of wind speed (a, b) and wind direction (c, d) recorded at the FINO1 met-mast station on August 13, 2015, at 20:30 UTC (a, c) and 22:00 UTC (b, d), data from WRF-meso (d01), WRF-LES (d02), WRF-SADLES (d03), LiDAR, and cup anemometers (Mast).

To gain a clearer understanding of the discrepancies between WRF-SADLES simulations and observations, we examine the vertical profiles of wind speed (Fig. 10a) and wind direction (Fig. 10b) at two key points in time. The first is 20:30 UTC when

360 the WRF-SADLES simulation shows the full wake effect. The second is 22:00 UTC when the full wake effect is observed in the data. At both times, the LiDAR data reveals a LLJ structure with a wind speed maximum of 17-20 m/s at around 300 meters. The observations of wind direction indicate wind veering, where the wind direction consistently turns clockwise with increasing height. However, within the overlapping region from 90 to 150 meters, some discrepancies exist between the two datasets. While the mast data exhibits consistency with the LiDAR data above 150 meters, the LiDAR wind directions below 365 150 meters may exhibit errors due to potential limitations in the retrieval algorithm or interference from the mast itself.

370 The mesoscale domain (D03) of the WRF model accurately replicates the observed LLJ event, capturing both its magnitude and the height of the wind speed maximum. However, the WRF-LES and WRF-SADLES simulations produce a weaker LLJ, with wind speeds 2-3 m/s lower. In terms of wind direction, the observations exhibit the highest vertical wind veer (approximately 8 degrees per 100 meters), followed by the mesoscale simulation (around 6 degrees per 100 meters). The WRF-LES simulations show the weakest vertical wind veer (about 4 degrees per 100 meters). The WRF-SADLES domain D05 performs slightly better than the WRF-LES domain D04 in capturing both wind speed and direction.

375 The full wake effect is observed when the wind direction approaches 90 degrees (easterly). At such times, the wake from the nearest Alpha Ventus turbine to the east reaches the FINO1 mast station. This is evident in both the observational wind speed (combining LiDAR and mast data) and the WRF-SADLES simulation, which show dips in wind speed. Notably, the wind speed profiles from the simulation and observations exhibit visually similar structures.

380 The mesoscale-to-microscale downscaling method proposed by Muñoz et al. Muñoz-Esparza et al. (2014) and in (Bakhoday-Paskyabi et al., 2022a) aimed to seamlessly transition atmospheric processes across scales. WRF-SADLES achieves this through nested simulations. However, in our case study (Fig. 10), WRF-LES simulations underestimated the strength of the LLJ, with the vertical wind veer only half of the observed values. This underestimation occurred in both the WRF-LES domain (D04, 200-meter resolution) and the WRF-SADLES domain (D04, 40-meter resolution).

385 We attribute this limitation to the resolution used in domain D04, which falls within the gray zone or 'terra incognita' for numerical models (Wyngaard, 2004). This zone represents a transition region between mesoscale and microscale, where traditional boundary layer parameterizations and LES are not accurately applicable. Here, turbulence activities may be misrepresented, leading to simulation inaccuracies. While WRF-SADLES simulations show some improvement, the small domain size likely restricts its ability to fully correct the erroneous environmental conditions inherited from the inflow boundaries of D04. We attempted to bypass this issue by skipping the 200-meter resolution domain. However, this resulted in WRF model failures, possibly due to the large grid ratio (1:25) not being supported.

390 Figure 11(a) shows the LOS velocity from a horizontal LiDAR scan from the FINO1 station at 23:00 UTC, at which the wind is blowing from the east and the full wake effect of a wind turbine from the Alpha Ventus is recorded. The LiDAR scan covers a circular sector extending from a height of 23.5 meters with a small elevation angle of 1.55 degrees, reaching a radius of 2500 meters and encompassing five turbines. The signal reaches a height of approximately 90 meters at the outer radius, corresponding to the hub height of the turbines. Turbine wakes are clearly visible, except for the middle turbine on the right, which is likely non-operational.

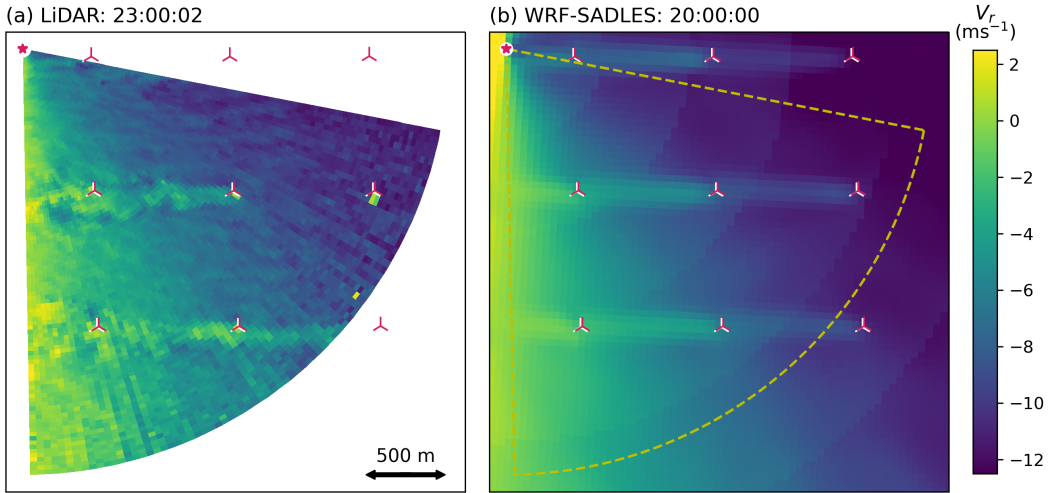


**Figure 11.** (a) Line-of-sight (LOS) velocity from a horizontal LiDAR scan at the FINO1 station around 23:00 UTC. (b) Simulated LOS velocity from from WRF-SADLES at 20:00 UTC.

For comparison, in Fig. 11b, the simulated LOS velocity from the WRF-SADLES model at 20:00 UTC with an easterly 395 wind direction is presented. Generally, there is good agreement between the model and LiDAR observations. Nevertheless, compared to the LiDAR data, the WRF-SADLES wind speed distribution is smoother. This is likely attributable to the coarse resolution to capture the small-scale turbulence explicitly.

#### 4.3 A brief example of farm-to-farm interaction

In this section, we briefly demonstrate the use of WRF-SADLES to simulate an example of farm-to-farm interaction. The LES 400 simulations were conducted for domains D04 and D05 from 06:00 UTC to 12:00 UTC on September 24, 2016. The mesoscale domains commenced earlier at 00:00 UTC to initialize the environmental conditions. This timeframe was selected due to the relatively steady wind direction from the south-southwest, allowing farm-to-farm interactions between Alpha Ventus and the wind farm to the southwest. To quantify the influence of this farm, we set up two experiments: the first experiment (EXP1) incorporated all four wind farms, while the second experiment (EXP2) excluded all wind farms except Alpha Ventus.

405 Figure 12a and b shows an example snapshot of the wind speed at the Alpha Ventus hub height (90 m) for the 40-meter LES domain for the two experiments at 10:00 UTC on September 24, 2016. Thanks to the cell perturbation at the southern boundary, the turbulence quickly becomes fully developed after a short distance from the southern border (or roughly ten percent of the domain width). This allows the turbulence flow to become quasi-steady when it reaches the turbines in the wind farms. Such turbulence development is important because it affects the wake recovery behind the turbines.

410 Figure 12c and d shows the four-hour average wind speed from 08:00 to 12:00 UTC on September 24, 2016. During this time window, the wind direction is relatively steady from the South-Southwest, enabling us to address the potential impact of

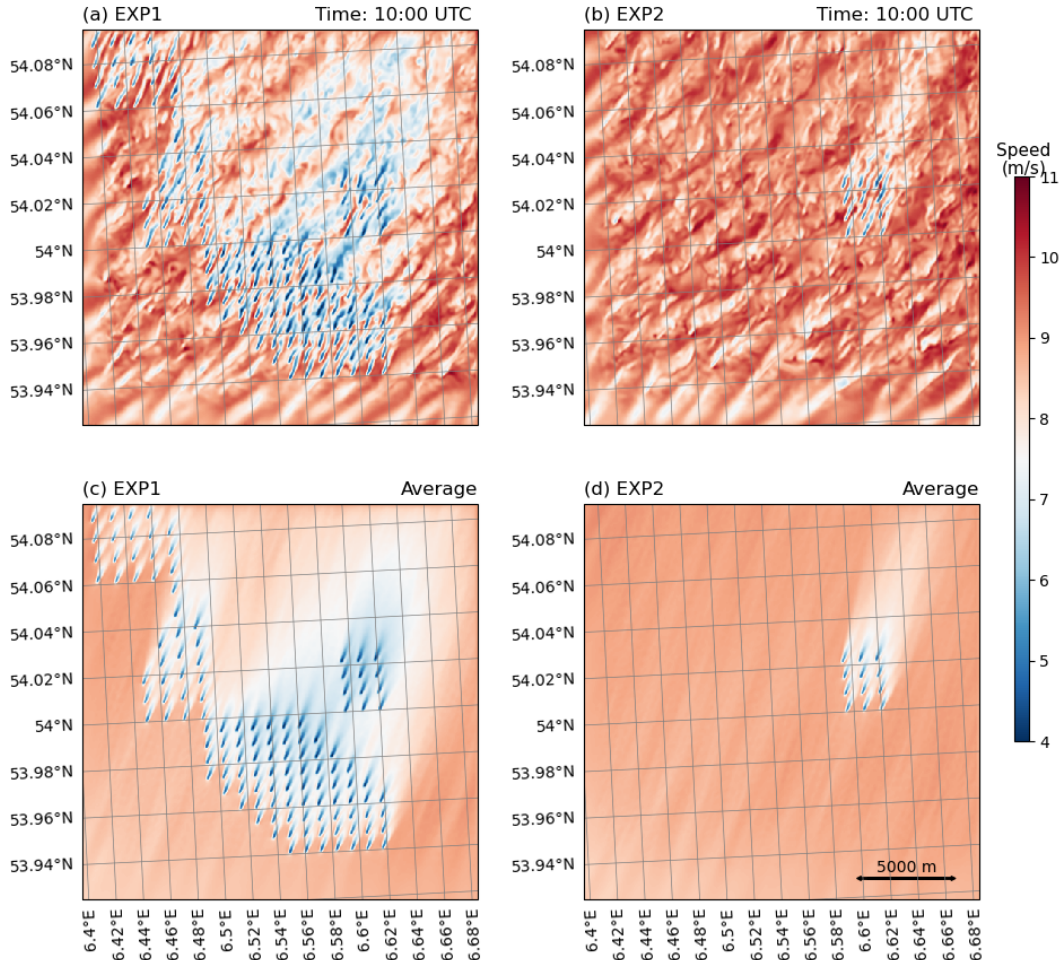


**Figure 12.** (a, b) A snapshot of wind speed in the 40-meter domain (D05) at the height of 90 meters at 10:00 UTC on September 24, 2016; (c, d) The 4-hour average wind speed (from 08:00 UTC to 12Z on September 24, 2016).

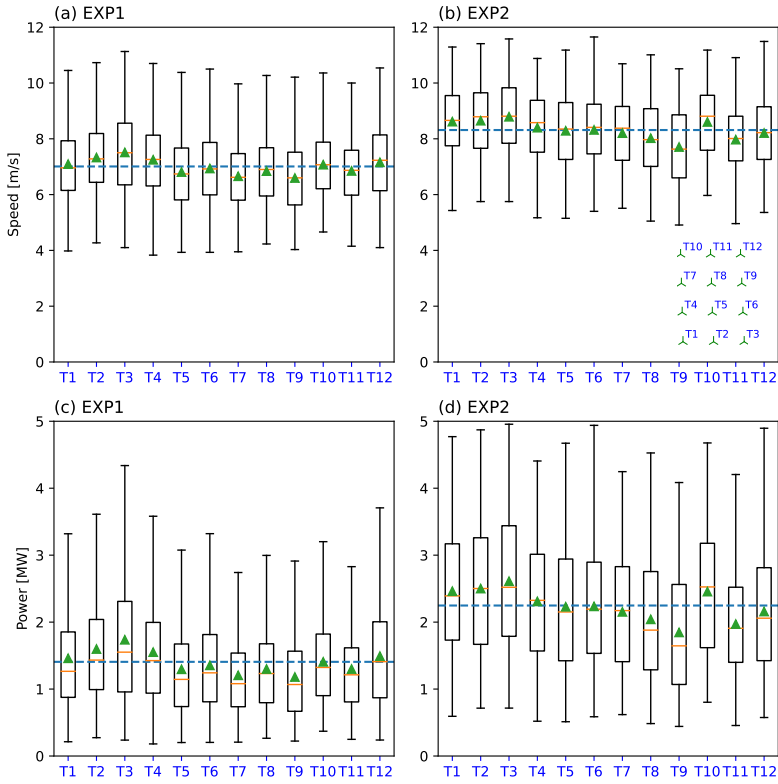


**Figure 13.** Box plots of 4 hours (from 08:00 to 12:00 UTC on September 24, 2016) for ambient wind speeds (a and b) and turbine powers (c and d) for the turbines in the Alpha Ventus wind farm. The average values (blue dashed lines) are 7 m/s and 8.3 m/s for (a) and (b), 1.4 MW and 2.25 MW for (c) and (d) respectively. The layout of the turbines in the Alpha Ventus wind farm is shown on the bottom right of panel (b).

turbine wakes in the Alpha Ventus wind farm. Before coming to the wind farm, the average speed is slightly above 8 m/s and is distributed uniformly because of the small size of the domain. In EXP1, the south-southwesterly wind direction and the wake from a nearby wind farm significantly reduce the wind speed reaching Alpha Ventus (Fig. 12c). Conversely, with no upstream 415 wind farm in EXP2, the averaged ambient wind speed remains nearly unchanged when approaching the Alpha Ventus wind farm. Consequently, the wake effect within Alpha Ventus is weaker in EXP1 compared to EXP2. This highlights the significant impact of farm-to-farm interaction, as evidenced by the larger difference in wind speed between the two scenarios compared to the variation within Alpha Ventus itself. In both experiments, the collective wave effects from the wind farm reduce the average wind speed to a distance over ten kilometers downstream.

420 Both experiments also show evidence of some intra-farm interaction where the wind speed deficits for turbines at the north-east corner are slightly smaller than those at the front south and west sides. However, due to the specific wind direction, the wakes generated by the turbines do not directly impact the turbines in the following rows. Consequently, the variation in wind

speed deficit between turbines within the Alpha Ventus wind farm is minimal compared to the overall difference between the two experiments.

425 Figure 13 also shows the intra-farm interaction is small compared to farm-to-farm interaction. For each experiment, the variation of the ambient wind speed is smaller than the difference between EXP1 and EXP2. The average ambient wind speed at the Alpha Ventus wind farm is significantly lower when the wind farm to the south presents (EXP1) compared to when there are none (EXP2). For EXP1, the average ambient wind speed is 7 m/s, as shown in Fig. 13a. In contrast, when there are 430 no nearby wind farms (EXP2), the average ambient wind speed is 8.3 m/s, as shown in Fig. 13b. This represents a reduction in wind speed of about 16%. However, due to the non-linear nature of the turbine power curve, the power reduction resulting from the farm-to-farm interaction (Fig. 13) is larger. The average power for EXP2 is approximately 2.25 MW, while the average power for EXP1 is 1.4 MW, corresponding to a reduction of about 38%.

## 5 Conclusion

In this paper, we presented our implementation of a Simple Actuator Disc model for Large Eddy Simulation (SADLES) within 435 the Weather Research and Forecast model (WRF-SADLES). Unlike other previous implementations of wind turbine parameterization within WRF, such as the General Actuator Disc (GAD) (Mirocha et al., 2014; Kale et al., 2022), WRF-SADLES only requires the power curve and thrust coefficient curve—the same information used in the wind farm parameterization (WFP Fitch et al., 2012) that is already included in WRF. The purpose of WRF-SADLES is to explicitly simulate the wakes of 440 multiple wind farms in nested downscaling applications from realistic atmospheric conditions. Therefore, the target resolution of the WRF-SADLES is in order of ten meters, which is lower than the resolutions of a few meters in typical applications using WRF-GAD (e.g., Mirocha et al., 2014; Kale et al., 2022), to reduce the computational demand.

WRF-SADLES employs the traditional actuator disc model, representing the turbine as a thin disc that generates thrust, slowing down ambient wind speed. In our idealized experiments with a single 5-MW turbine (Section 3), WRF-SADLES demonstrated good agreement compared to a dedicated LES model (the PALM model), whose actuator disc model uses the 445 blade element theory, providing a more comprehensive representation. Interestingly, at our target resolution of 30 meters, WRF-SADLES exhibited better agreement with the 10-meter resolution than the PALM model.

We assessed two methods for evaluating the axial induction factor: direct evaluation (Option 1) using data points at and in front of the turbine, and inferred evaluation (Option 2) using 1D momentum theory. The results demonstrated strong agreement 450 between the two methods. We recommend employing Option 2 to avoid potential issues associated with Option 1, as discussed in Section 2.1.

Additionally, we experimented with adding subgrid-scale turbulence kinetic energy (TKE) at the actuator disc, similar to the approach by Fitch et al. (2012). However, the effect of added TKE only influenced a short distance from the turbine, and the far wake structures, including wake deficit and turbulent intensity, remained similar regardless of the presence of added TKE. Therefore, we recommend deactivating this option (i.e.  $f_{TKE} = 0$ ) for practical application, partly because the rationale 455 behind the method does not reflect reality.

We conducted a brief validation of WRF-SADLES using observational data from the FINO1 offshore meteorological mast station. This data included measurements from a cup anemometer at 90 meters height, as well as vertical and horizontal wind profiles obtained by LiDAR. The simulation downscals the ERA5 global reanalysis from a coarse resolution (approximately 31 kilometers) to a turbine scale resolution (40 meters). This downscaling is achieved through a system of five nested domains, 460 with the outer three domains simulating mesoscale processes and the two inner domains simulating eddy turbulence. The results demonstrate good agreement in the wake deficit observed at the FINO1 location between WRF-SADLES and the actual observations. However, there is a discrepancy in the timing of the wake deficit occurrence. We attribute this error not to the turbine model itself, but to the intermediate 200-meter resolution LES domain. This domain serves as the transitional zone between mesoscale and microscale, where turbulence activity is not accurately represented.

465 Finally, we present an example of farm-to-farm interaction at the Alpha Ventus wind farm near the FINO1 station. Here, the wind farm to the southeast of Alpha Ventus leads to a reduction in ambient wind speed by approximately 16%, resulting in an average turbine power decrease of 38% during a 4-hour analysis window.

We've made our code openly available to promote further research in wind energy. Our code distribution includes our implementation of the cell perturbation method (Muñoz-Esparza et al., 2014), crucial for turbulence development in nested 470 LES. While WRF-SADLES demonstrates promising capabilities for meso-to-micro downscaling, addressing issues in the transition resolutions will be crucial for enhancing wake predictions. Future development areas for WRF-SADLES could involve implementing yaw misalignment to enable wake deflection and investigating turbine yaw control strategies.

## Appendix A: Additional WRF namelist options

**Table A1.** Summary of WRF-SADLES namelist options

Namelist options (&physics)	Default value	Description
sadles_opt (max_domains)	0	=0 turn off SADLES for the current domain; =1 or 2: use Option 1 (direct) or Option 2 (inferred) for the induction factor, respectively
sadles_startmin (max_domains)	0	Time to start SADLES in minutes
sadles_maxradius *	120	Max turbine radius in meter,
sadles_mindx *	20	Min $\Delta x$ in meter,
sadles_mindz *	20	Min $\Delta z$ in meter,
sadles_tkefact	0.5	$f_{KTE}$ , from 0 to 1 (see the text for the description)
ideal_f	0.0001	Coriolis force (em_les only),
ideal_znt	-1.	Surface roughness length (em_les only, only effective for positive values).

\* These values are used to allocate arrays within the SADLES module.

**Table A2.** Summary of cell perturbation namelist options

Namelist options (&cpert)	Default value	Description
cell_pert_xs (max_domains)	0	=1 will apply cell perturbation for the western boundary
cell_pert_xe (max_domains)	0	=1 will apply cell perturbation for the eastern boundary
cell_pert_ys (max_domains)	0	=1 will apply cell perturbation for the southern boundary
cell_pert_ye (max_domains)	0	=1 will apply cell perturbation for the northern boundary
cell_pert_magnitude	0.5	Magnitude of the cell perturbation
cell_pert_interval (max_domains) *	320	Interval to apply the perturbation in seconds
cell_pert_k1	8	Bottom level of the transition layer for cell perturbation
cell_pert_k2	16	Top level of the transition layer for cell perturbation

\* The interval should be approximately  $\frac{8\Delta x}{U}$ , where  $U$  is the average wind speed during the simulation. For example, with  $\Delta x = 200$  m and  $U = 5$  m/s, the interval will be approximately  $\frac{8(200\text{ m})}{5\text{ m/s}} = 320$  s.

*Code and data availability.*

475 Our WRF-SADLES Version 1.2, along with a concise user's guide and an example of idealized settings for the 30-meter simulation, can be downloaded from: <https://doi.org/10.5281/zenodo.10803669> (Bui, 2023). For the latest version of the WRF-SADLES user's guide, refer to the GitHub repository: <https://github.com/haibuihoang/WRF-SADLES>.

480 The WRF-ARW model is available for download from <https://github.com/wrf-model/WRF>, while the PALM model can be accessed at [https://gitlab.palm-model.org/releases/palm\\_model\\_system](https://gitlab.palm-model.org/releases/palm_model_system). Snapshots of WRF-v4.3.1 and PALM-v21.10 can be obtained from: <https://doi.org/10.5281/zenodo.8054487>.

The ERA5 hourly reanalysis data can be downloaded from: <https://cds.climate.copernicus.eu/>. Turbine information is also available for download at: <https://doi.org/10.5281/zenodo.4668613> (Larsén and Fischereit, 2021).

485 *Author contributions.* Hai Bui proposed and implemented the WRF-SADLES code, conducted the WRF-SADLES simulations, and wrote the manuscript. Mostsafa provided turbine information, revised the manuscript, and assisted with several technical discussions. Mohammadmreza contributed by writing the description of the PALM model, performing the PALM simulation, and assisting with manuscript revisions.

*Competing interests.* All authors declare that they have no competing of interest.

490 *Acknowledgements.* The work is a part of the HIghly advanced Probabilistic design and Enhanced Reliability methods for high-value, cost-efficient offshore WIND (HIPERWIND) project, which has received funding from the European Union's Horizon 2020 Research and Innovation Programme under Grant Agreement No. 101006689. The simulations were performed on resources provided by projects NN9871K and NN9696K by UNINETT Sigma2 - the National Infrastructure for High Performance Computing and Data Storage in Norway.

## References

- Anderson, C.: Wind turbines: Theory and practice, Cambridge University Press, 2020.
- Ardillon, E., Paskyabi, M. B., Cousin, A., Dimitrov, N., Dupoiron, M., Eldevik, S., Fekhari, E., Ferreira, C., Guiton, M., Jezequel, B., et al.:  
495 Turbine loading and wake model uncertainty, Deliverable D3.2 for HIPERWIND project, <https://www.hiperwind.eu/>, 2023.
- Arthur, R. S., Mirocha, J. D., Marjanovic, N., Hirth, B. D., Schroeder, J. L., Wharton, S., and Chow, F. K.: Multi-scale simulation of wind farm performance during a frontal passage, *Atmosphere*, 11, 245, 2020.
- Bakhoday-Paskyabi, M., Bui, H., and Mohammadpour Penchah, M.: Atmospheric-Wave Multi-Scale Flow Modelling, Deliverable D2.1 for HIPERWIND project, <https://www.hiperwind.eu/>, 2022a.
- 500 Bakhoday-Paskyabi, M., Krutova, M., Bui, H., and Ning, X.: Multiscale Simulation of Offshore Wind Variability During Frontal Passage: Brief Implication on Turbines' Wakes and Load, in: *Journal of Physics: Conference Series*, vol. 2362, p. 012003, IOP Publishing, 2022b.
- Baldauf, M., Seifert, A., Förstner, J., Majewski, D., Raschendorfer, M., and Reinhardt, T.: Operational convective-scale numerical weather prediction with the COSMO model: Description and sensitivities, *Monthly Weather Review*, 139, 3887–3905, 2011.
- Breton, S.-P., Sumner, J., Sørensen, J. N., Hansen, K. S., Sarmast, S., and Ivanell, S.: A survey of modelling methods for high-fidelity wind farm simulations using large eddy simulation, *Philosophical Transactions of the Royal Society A: Mathematical, Physical and Engineering Sciences*, 375, 20160 097, 2017.
- Bui, H.: Simple Actuator Disc for Large Eddy Simulation (SADLES), <https://doi.org/10.5281/zenodo.10803669>, 2023.
- Bui, H. and Bakhoday-Paskyabi, M.: Mesoscale Simulation of Open Cellular Convection: Roles of Model Resolutions and Physics Parameterizations, in: *Journal of Physics: Conference Series*, vol. 2362, p. 012006, IOP Publishing, 2022.
- 510 Burton, T., Jenkins, N., Sharpe, D., and Bossanyi, E.: Wind energy handbook, John Wiley & Sons, 2011.
- Calaf, M., Meneveau, C., and Meyers, J.: Large eddy simulation study of fully developed wind-turbine array boundary layers, *Physics of fluids*, 22, 015 110, 2010.
- Churchfield, M., Wang, Q., Scholbrock, A., Herges, T., Mikkelsen, T., and Sjöholm, M.: Using high-fidelity computational fluid dynamics to help design a wind turbine wake measurement experiment, in: *Journal of Physics: Conference Series*, vol. 753, p. 032009, IOP Publishing,  
515 2016.
- Crespo, A., Herna, J., et al.: Turbulence characteristics in wind-turbine wakes, *Journal of wind engineering and industrial aerodynamics*, 61, 71–85, 1996.
- Deardorff, J. W.: Stratocumulus-capped mixed layers derived from a three-dimensional model, *Boundary-layer meteorology*, 18, 495–527, 1980.
- 520 Dörenkämper, M., Witha, B., Steinfeld, G., Heinemann, D., and Kühn, M.: The impact of stable atmospheric boundary layers on wind-turbine wakes within offshore wind farms, *Journal of Wind Engineering and Industrial Aerodynamics*, 144, 146–153, 2015.
- Fischereit, J., Brown, R., Larsén, X. G., Badger, J., and Hawkes, G.: Review of Mesoscale Wind-Farm Parametrizations and Their Applications, *Boundary-Layer Meteorology*, 182, 175–224, 2022.
- Fitch, A. C., Olson, J. B., Lundquist, J. K., Dudhia, J., Gupta, A. K., Michalakes, J., and Barstad, I.: Local and mesoscale impacts of wind farms as parameterized in a mesoscale NWP model, *Monthly Weather Review*, 140, 3017–3038, 2012.
- Fleming, P. A., Gebraad, P. M., Lee, S., van Wingerden, J.-W., Johnson, K., Churchfield, M., Michalakes, J., Spalart, P., and Moriarty, P.:  
525 Evaluating techniques for redirecting turbine wakes using SOWFA, *Renewable Energy*, 70, 211–218, 2014.

- Gaertner, E., Rinker, J., Sethuraman, L., Zahle, F., Anderson, B., Barter, G. E., Abbas, N. J., Meng, F., Bortolotti, P., Skrzypinski, W., et al.: IEA wind TCP task 37: definition of the IEA 15-megawatt offshore reference wind turbine, Tech. rep., National Renewable Energy 530 Lab.(NREL), Golden, CO (United States), 2020.
- Göçmen, T., Van der Laan, P., Réthoré, P.-E., Diaz, A. P., Larsen, G. C., and Ott, S.: Wind turbine wake models developed at the technical university of Denmark: A review, *Renewable and Sustainable Energy Reviews*, 60, 752–769, 2016.
- Hersbach, H., Bell, B., Berrisford, P., Hirahara, S., Horányi, A., Muñoz-Sabater, J., Nicolas, J., Peubey, C., Radu, R., Schepers, D., et al.: The ERA5 global reanalysis, *Quarterly Journal of the Royal Meteorological Society*, 146, 1999–2049, 2020.
- Hong, S.-Y., Noh, Y., and Dudhia, J.: A new vertical diffusion package with an explicit treatment of entrainment processes, *Mon. Weather Rev.*, 134, 2318–2341, 2006.
- Iacono, M. J., Delamere, J. S., Mlawer, E. J., Shephard, M. W., Clough, S. A., and Collins, W. D.: Radiative forcing by long-lived greenhouse gases: Calculations with the AER radiative transfer models, *J. Geophys. Res. Atmos.*, 113, 2008.
- Jiménez, P. A., Dudhia, J., González-Rouco, J. F., Navarro, J., Montávez, J. P., and García-Bustamante, E.: A revised scheme for the WRF 540 surface layer formulation, *Monthly weather review*, 140, 898–918, 2012.
- Jonkman, J., Butterfield, S., Musial, W., and Scott, G.: Definition of a 5-MW reference wind turbine for offshore system development, Tech. rep., National Renewable Energy Lab.(NREL), Golden, CO (United States), 2009.
- Kale, B., Buckingham, S., van Beeck, J., and Cuerva-Tejero, A.: Implementation of a generalized actuator disk model into WRF v4. 3: A validation study for a real-scale wind turbine, *Renewable Energy*, 197, 810–827, 2022.
- Kumer, V.-M., Reuder, J., and Furevik, B. R.: A comparison of LiDAR and radiosonde wind measurements, *Energy Procedia*, 53, 214–220, 545 2014.
- Larsén, X. G. and Fischereit, J.: A case study of wind farm effects using two wake parameterizations in WRF (V3.7.1) in the presence of low level jets, <https://doi.org/10.5281/zenodo.4668613>, 2021.
- Ledoux, J., Riffo, S., and Salomon, J.: Analysis of the blade element momentum theory, *SIAM Journal on Applied Mathematics*, 81, 2596–550 2621, 2021.
- Lee, J. C. and Lundquist, J. K.: Evaluation of the wind farm parameterization in the Weather Research and Forecasting model (version 3.8. 1) with meteorological and turbine power data, *Geoscientific Model Development*, 10, 4229–4244, 2017.
- Lilly, D. K.: The representation of small-scale turbulence in numerical simulation experiments, *IBM Form*, pp. 195–210, 1967.
- Lin, D., Khan, B., Katurji, M., Bird, L., Faria, R., and Revell, L. E.: WRF4PALM v1. 0: a mesoscale dynamical driver for the microscale 555 PALM model system 6.0, *Geoscientific Model Development*, 14, 2503–2524, 2021.
- Maronga, B., Gryschka, M., Heinze, R., Hoffmann, F., Kanani-Sühring, F., Keck, M., Ketelsen, K., Letzel, M. O., Sühring, M., and Raasch, S.: The Parallelized Large-Eddy Simulation Model (PALM) version 4.0 for atmospheric and oceanic flows: model formulation, recent developments, and future perspectives, *Geoscientific Model Development*, 8, 2515–2551, 2015.
- Maronga, B., Banzhaf, S., Burmeister, C., Esch, T., Forkel, R., Fröhlich, D., Fuka, V., Gehrke, K. F., Geletič, J., Giersch, S., et al.: Overview 560 of the PALM model system 6.0, *Geoscientific Model Development*, 13, 1335–1372, 2020.
- Mirocha, J., Kosovic, B., Aitken, M., and Lundquist, J.: Implementation of a generalized actuator disk wind turbine model into the weather research and forecasting model for large-eddy simulation applications, *Journal of Renewable and Sustainable Energy*, 6, 013 104, 2014.
- Moeng, C.-H. and Wyngaard, J. C.: Spectral analysis of large-eddy simulations of the convective boundary layer, *Journal of Atmospheric Sciences*, 45, 3573–3587, 1988.

- 565 Mukul Tewari, N., Tewari, M., Chen, F., Wang, W., Dudhia, J., LeMone, M., Mitchell, K., Ek, M., Gayno, G., Wegiel, J., et al.: Implementation and verification of the unified NOAH land surface model in the WRF model (Formerly Paper Number 17.5), in: Proceedings of the 20th Conference on Weather Analysis and Forecasting/16th Conference on Numerical Weather Prediction, Seattle, WA, USA, vol. 14, 2004.
- Muñoz-Esparza, D., Kosović, B., Mirocha, J., and van Beeck, J.: Bridging the transition from mesoscale to microscale turbulence in numerical weather prediction models, *Boundary-layer meteorology*, 153, 409–440, 2014.
- 570 Muñoz-Esparza, D., Kosović, B., Van Beeck, J., and Mirocha, J.: A stochastic perturbation method to generate inflow turbulence in large-eddy simulation models: Application to neutrally stratified atmospheric boundary layers, *Phys. Fluids*, 27, 035102, 2015.
- Ning, X., Paskyabi, M. B., Bui, H. H., and Penchah, M. M.: Evaluation of sea surface roughness parameterization in meso-to-micro scale simulation of the offshore wind field, *Journal of Wind Engineering and Industrial Aerodynamics*, 242, 105592, 2023.
- Onel, H. C. and Tuncer, I. H.: Short-Term Numerical Forecasting of Near-Ground Wind Fields Using OpenFOAM Coupled With WRF, in: 575 AIAA SCITECH 2023 Forum, p. 1737, 2023.
- Porté-Agel, F., Bastankhah, M., and Shamsoddin, S.: Wind-turbine and wind-farm flows: A review, *Boundary-layer meteorology*, 174, 1–59, 2020.
- Pryor, S. C., Shepherd, T. J., Volker, P. J., Hahmann, A. N., and Barthelmie, R. J.: “Wind Theft” from onshore wind turbine arrays: sensitivity to wind farm parameterization and resolution, *Journal of Applied Meteorology and Climatology*, 59, 153–174, 2020.
- 580 Quarton, D. and Ainslie, J.: Turbulence in wind turbine wakes, *Wind Engineering*, pp. 15–23, 1990.
- Rankine, W. J. M.: On the mechanical principles of the action of propellers, *Transactions of the Institution of Naval Architects*, 6, 1865.
- Saiki, E. M., Moeng, C.-H., and Sullivan, P. P.: Large-eddy simulation of the stably stratified planetary boundary layer, *Boundary-Layer Meteorology*, 95, 1–30, 2000.
- 585 Salim, M. H., Schluenzen, K. H., Grawe, D., Boettcher, M., Gierisch, A. M., and Fock, B. H.: The microscale obstacle-resolving meteorological model MITRAS v2. 0: model theory, *Geoscientific Model Development*, 11, 3427–3445, 2018.
- Skamarock, W. C., Klemp, J. B., Dudhia, J., Gill, D. O., Liu, Z., Berner, J., Wang, W., Powers, J. G., Duda, M. G., Barker, D. M., et al.: A description of the advanced research WRF model version 4, *National Center for Atmospheric Research: Boulder, CO, USA*, 145, 145, 2019.
- Thompson, G., Field, P. R., Rasmussen, R. M., and Hall, W. D.: Explicit forecasts of winter precipitation using an improved bulk microphysics scheme. Part II: Implementation of a new snow parameterization, *Mon. Weather Rev.*, 136, 5095–5115, 2008.
- 590 Volker, P., Badger, J., Hahmann, A. N., and Ott, S.: The Explicit Wake Parametrisation V1. 0: a wind farm parametrisation in the mesoscale model WRF, *Geoscientific Model Development*, 8, 3715–3731, 2015.
- Vollmer, L., van Dooren, M., Trabucchi, D., Schneemann, J., Steinfeld, G., Witha, B., Trujillo, J., and Kühn, M.: First comparison of LES of an offshore wind turbine wake with dual-Doppler lidar measurements in a German offshore wind farm, in: *Journal of Physics: Conference Series*, vol. 625, p. 012001, IOP Publishing, 2015.
- 595 Wang, Q., Luo, K., Yuan, R., Wang, S., Fan, J., and Cen, K.: A multiscale numerical framework coupled with control strategies for simulating a wind farm in complex terrain, *Energy*, 203, 117913, 2020.
- Witha, B., Steinfeld, G., and Heinemann, D.: High-resolution offshore wake simulations with the LES model PALM, in: *Wind energy-impact of turbulence*, pp. 175–181, Springer, 2014.
- 600 Wyngaard, J. C.: Toward numerical modeling in the “Terra Incognita”, *Journal of the atmospheric sciences*, 61, 1816–1826, 2004.
- Zhang, C., Wang, Y., and Hamilton, K.: Improved representation of boundary layer clouds over the southeast Pacific in ARW-WRF using a modified Tiedtke cumulus parameterization scheme, *Mon. Weather Rev.*, 139, 3489–3513, 2011.